IMPLICATIONS OF HEAVY-ION-INDUCED SATELLITE X-RAY EMISSION. II*

Production of K and L X rays by 0.9-2.6 MeV/u Ar Ions in thick targets of V, Cu, Nb, Ta, and Pt

CONF-830772--4

DE83 015681

G.D. O'KELLEY, R.L. AUBLE, L.D. HULETT, H.J. KIM, W.T. MILNER, S. RAMAN, O. SHAHAL†, C.R. VANE and J.P. YOUNG

Oak Ridge National Laboratory, Oak Ridge, Tennessee 37830

G. LAPICKI

Department of Physics, East Carolina University,

Greenville, North Carolina 27384

Cross sections are reported for X-ray production in targets of $_{23}V$, $_{29}Cu$, $_{41}Nb$, $_{73}Ta$, and $_{78}Pt$ by ^{40}Ar ions of 36.0, 56.4, 76.6, and 103 MeV. Because the targets were relatively thick, ~ 1 mg/cm^2, the data were corrected, using a novel approach, for projectile energy loss and X-ray attenuation in the targets. The cross sections so analyzed are compared with the predictions of the first Born approximation as well as with those of a more extensive treatment which includes energy loss, Coulomb deflection, perturbed stationary-state, and relativistic effects. The significant discrepancies between the data and this latter theory are attributed primarily to the influence of multiple ionization on the X-ray emission probabilities.

*Research sponsored by the Division of Basic Energy Sciences, U.S. Department of Energy, under Contract No. W-7405-eng-26 with the Union Carbide Corporation. Accordingly, the U.S. government retains a non-exclusive, royalty-free license to publish or reproduce the published form of this contribution, or allow others to do so, for U.S. government purposes.

†Visitor from Nuclear Research Centre-Negev, Beer-Sheva, Israel

1. Introduction

The work described here was carried out as a necessary first step in the design of a high-resolution experiment to study the implications of variations in heavy-ion-induced X-ray satellite spectra. For this purpose, one needs X-ray production cross sections as a function of energy for various targets. We were unable to find in the literature any measured cross sections for X-ray production by $^{40}_{18}Ar$ ions of ~ 1 MeV/u.

An abundance of data does exist for X-ray production cross sections in inner shell ionization [1]; however, most of these data were taken with light projectiles such as protons or alpha particles. There is a paucity of data on systems characterized by $0.3 \lesssim Z_1/Z_2 \lesssim 1$, where Z_1 denotes the atomic number of projectile and Z_2 the atomic number of the target atom. In these systems, the most interesting range of projectile velocities lies well above one atomic unit of velocity (speed of light/137) but not much larger than the orbital velocity of the electron to be removed from the inner shell. These conditions can be attained with $^{40}_{18}Ar$ ions of ~ 1 MeV/u. Such considerations led us to choose a beam of $^{40}_{18}Ar$ ions in the energy range 36-103 MeV for measurements of K X-rays from $_{23}V$, $_{29}Cu$, and $_{41}Nb$, as well as L X-rays from $_{41}Nb$, $_{73}Ta$, and $_{78}Pt$.

Because our ultimate goal was to study chemical compounds that were likely to be in the form of thick targets, all of the targets in the present experiments were of a convenient thickness, $\lesssim 1$ mg/cm^2. The objective was to determine X-ray cross sections for comparison with theory. To obtain them, the thick-target yields were converted to cross sections and corrected for the finite energy loss by the projectile and for the self-

attenuation of the X-rays produced in the targets. The target X-ray cross sections were then compared with the predictions of the first Born approximation and with those of a more complete theory.

2. Experimental procedures and data analysis

Measurements were performed at the Oak Ridge Isochronous Cyclotron (ORIC), using ion beams of $^{40}_{18}Ar^{q+}$ with energies of 36.0, 56.4, 76.6, and 103 MeV, and respectively, with charge states q of 4, 5, 6, and 7. The geometry of the experiment is shown in fig. 1. The beam from ORIC was collimated to a diameter of 2 mm by a graphite aperture, sent through selected metallic targets at an angle of 45°, then passed to a Faraday cup. The targets of natural isotopic composition (with thicknesses in mg/cm^2) were: $_{23}V$ (0.830), $_{29}Cu$ (0.887), $_{41}Nb$ (0.744), $_{73}Ta$ (0.957), and $_{78}Pt$ (0.927). The ions, scattered elastically at a laboratory angle of 35° to the beam direction, were collimated by another 2 mm Ta aperture placed directly in front of a silicon surface-barrier semiconductor detector located 36.3 mm from the target. Based on the number of counts, N_p, registered in this particle detector, an absolute normalization of the incident beam intensity was made as described below.

The X-ray counts, N_X, were measured in a Si(Li) detector placed at 90° to the direction of the beam or 45° with respect to the target surface. At low (~ 10^3 c/s) counting rates, the detector was capable of a resolution of 150 eV full width at half maximum at an energy of 5.895 keV; in most of our experiments the resolution was somewhat poorer because of the high (~ 10^4 c/s) counting rates encountered. The X-rays emerged from the vacuum chamber through a 0.51 mg/cm^2 Mylar window and passed a short distance (~ 1 mm) in

air before striking the 2.35 mg/cm^2 Be window of the Si(Li) detector. The absolute efficiency of the X-ray detector, ε_X, as a function of photon energy was determined in the energy range of 6-60 keV by use of radioactive standards of ^{55}Fe, ^{241}Am, and ^{133}Ba that had approximately the same diameter as the beam and were mounted at the target position. Below 5.895 keV, attenuation factors for the Mylar and Be windows and air were calculated from published photon cross sections [2]. It is estimated that the values of ε_X used in this work are accurate to ± 7%.

The observed X-ray production cross sections, σ_X^{obs}, can be extracted from the measured yields N_p/τ_p and N_X/τ_X, according to

$$\sigma_X^{obs} = \frac{N_X}{\varepsilon_X \tau_X} \cdot \frac{\tau_p}{N_p} \cdot \left(\frac{d\sigma}{d\Omega}\right)_p \Delta\Omega, \qquad (1)$$

where τ_p and τ_X are the livetimes of the particle and X-ray measurements, respectively, $(d\sigma/d\Omega)_p$ is the differential cross section for elastic scattering of particles, and $\Delta\Omega$ is the solid angle of the particle detector. The quantity $(d\sigma/d\Omega)_p$ was evaluated as the Rutherford cross section for the appropriate projectile-target combination at the energy of the incident beam E_1, and at the laboratory angle of 35°.

To verify that the elastic scattering cross section is indeed given by the Rutherford cross section for all the cases investigated, we consulted the results [3] of an optical model calculation for the case most prone to deviation from Rutherford scattering, namely, 103-MeV $^{40}_{18}$Ar projectiles on a $_{23}$V target. The calculated cross sections were equal to the Rutherford cross sections within 0.1% for all laboratory scattering angles

<50°. Thus, we conclude that the normalization procedure just described is adequate for the projectile-target combinations used in our experiments.

Because of the finite thickness of the targets, t, σ_X^{obs} must be corrected for the projectile energy loss and for the X-ray self-attenuation, μ, in the target [4]. With $R_0(E_1)$ as the projected range in the target material, the projectile energy decreases from E_1 to $E(R_0-z)$ after traversal through a distance z in the target. The X-rays produced at z are self-attenuated over the distance $z\cdot\cos\theta/\cos\phi$ (see Fig. 1). If σ_X is the unattenuated X-ray production cross section per target atom for projectiles of energy $E(R_0-z)$, then

$$\sigma_X^{obs}(E_1) = \frac{1}{t'}\int_0^{t'} e^{-\mu' z}\sigma_X[E(R_0-z)]dz \qquad (2)$$

where $t' \equiv t/\cos\theta$ is the effective target thickness and $\mu' \equiv \mu\cos\theta/\cos\phi$ is the effective target X-ray self-attenuation mass coefficient. As sketched in fig. 1, both angles θ and ϕ are fixed at 45° so that, in our experiment, $t' = \sqrt{2}\,t$ and $\mu' = \mu$. Values of μ used in the data analysis are included in table 1.

For comparison with theory, one should deconvolute σ_X from eq. (2) in terms of σ_X^{obs}, μ',t', and some mean value of the energy loss in the target, $\overline{\Delta E}$. Such a deconvolution is possible for the present cases, since $\overline{\Delta E} \ll E_1$ for a 100-MeV projectile; for 36-MeV ion beams $\overline{\Delta E}/E_1$ is still less than 0.22 (see table 1). In Appendix A we discuss the procedure used to obtain cross sections evaluated at $E_1-\overline{\Delta E}$ from the σ_X^{obs} values measured at E_1. The resulting cross sections, $\sigma_X(E_1-\overline{\Delta E})$, are discussed below and

are the cross sections to be compared with theoretical predictions at energies $E_1-\overline{\Delta E}$.

3. Results

Observed X-ray spectra produced at the lowest bombarding energy, 36.0 MeV, are shown in fig. 2, while those at the highest energy, 103 MeV, are shown in fig. 3. As expected, a prominent feature of all spectra is the peak at 3 keV, the $K_{\alpha 1,2}$ line from excitation of the Ar projectile. Above, and not well resolved from the Ar $K_{\alpha 1,2}$ line, is a weak Ar K_β peak. The higher-energy portions of the X-ray spectra of $_{23}V$, $_{29}Cu$, and $_{41}Nb$ show qualitatively the decrease in production of K X-rays as the atomic number of the target increases. For $_{73}Ta$ and $_{78}Pt$, only the L- and M-series X-rays characteristic of these targets can be identified.

The X-ray cross sections, σ_X^{obs}, calculated according to eq. 1, are listed in tables 2 and 3. It should be noted that these values are characteristic of the particular target thickness, and do not include corrections for projectile energy loss and X-ray self-attenuation in the target. Cross sections, σ_X, evaluated at an energy $E_1-\overline{\Delta E}$ were calculated according to the prescription described earlier and discussed in greater detail in Appendix A. These cross sections are displayed on the right-hand sides of tables 2 and 3 for energies $E_1-\overline{\Delta E}$, and as such they may be compared conveniently with the uncorrected cross sections, σ_X^{obs}, obtained at incident energies E_1.

The trends in the values of σ_X are shown graphically in figs. 4-9 for production of K- and L-series X-rays for all five targets investigated. As mentioned before, no prior experimental data existed in the literature

for the same projectile-target combination and for similar $^{40}_{18}Ar$ projectile energies. Meanwhile, Tanis, Jacobs, and Shafroth [5] have investigated the production of K X-rays from $_{29}Cu$ targets irradiated with 20-80 MeV $_{17}Cl$ ions. Their targets were thin (20-220 $\mu g/cm^2$) and their data were extrapolated to zero target thickness. In fig. 5, the cross sections of [5] for the $_{17}Cl + _{29}Cu$ system are compared with our data for the $_{18}Ar + _{29}Cu$ system, both plotted with the same MeV/u abscissa. Even though the two data sets cannot be directly compared, they are quite similar, both in magnitude of the cross sections and in the shape of the energy dependence, in spite of the wide differences in target thicknesses and in the methods for extraction of zero target thickness cross sections from the data.

A number of sources of error could be quantified in the calculations of σ_X^{obs} and σ_X. As an example of experimental uncertainties for a particular case, K_α X-rays produced in a $_{41}Nb$ target by a 76.6-MeV argon beam are listed in table 4. Although in table 4 we take the typical uncertainty in μ to be 15%, its effect on the correction factor for self absorption, C_X, is small. Two significant sources of experimental error are the efficiency of the X-ray detector, ε_X, and variations in the thickness of the metal target. As stated earlier, the combined error in ε_X was estimated to be 7%. The nonuniformities of the target foils were determined by a method which employed X-ray fluorescence [6]. The results of the measurements for each target foil (average uncertainties in thickness are in parentheses) were: vanadium (4%), copper (5%), niobium (7%), tantalum (7%), and platinum (6%). In table 4 it can be seen that the error in σ_X^{obs} is primarily influenced by the uncertainty in ε_X, but the error in

σ_X is influenced most strongly by a combined propagation of errors in t and S. A 7% uncertainty in each one of these quantities results in a 20-25% uncertainty in the C_R correction factor (see Appendix A).

4. Comparison with theories

Although a comprehensive calculation of the X-ray production in the projectile-target systems investigated here would be of great interest, such a treatment is beyond the scope of the present work. Instead, we will compare our results with the predictions of perturbative theories. Even for relatively large Z_1/Z_2 values, these theories are more appropriate than molecular orbital calculations, particularly outside the slow collision regime.

To compare X-ray production data with the predictions of ionization theories, all ionization cross sections $\sigma_{S'}$ that contribute to the creation of a vacancy in an S shell are added after multiplication by $\nu^{S'}$, the probability for S X-ray emission while the S' vacancy is to be filled. For $K = K_\alpha + K_\beta$ x-ray production, $\nu_K \equiv \omega_K$, the K-shell X-ray fluorescence yield; for $L_{\alpha'}$, $L_{\beta'}$, L_ℓ X-rays, ν_L are deduced from the fluorescence yields, Coster-Kronig transition rates, and branching ratios for a particular X-ray. We use the fluorescence yields and Coster-Kronig transition rates recommended by Krause [7] and the L-subshell X-ray emission probabilities derived from the work of Scofield [8] for systems with a single-electron vacancy. In the K shell, the ω_K values are 0.243, 0.440, 0.747 for $_{23}V$, $_{29}Cu$, and $_{41}Nb$, respectively. In the L-shell,

$$\sigma_{LX} = \nu_L^{L1} \cdot \sigma_{L_1} + \nu_L^{L2} \cdot \sigma_{L_2} + \nu_L^{L3} \cdot \sigma_{L_3}. \qquad (3)$$

The ν values are listed in table 5.

The appropriate ionization cross sections have been evaluated according to the first Born approximation [9,10] as well as to the ECPSSR approach [11,12]. This latter approach goes beyond the first Born approximation in that it accounts for energy-loss (E), Coulomb-deflection (C), perturbed-stationary state (PSS), and relativistic (R) effects which are not dealt with in the standard theories using the first Born approximation. In both theories, we calculate the ionization cross section as the sum of the cross sections for direct ionization to the continuum of the target atom plus electron capture to unoccupied bound states of the projectile. In the first Born treatments, this requires the nonrelativistic, plane-wave Born approximation (PWBA) [9] for direct ionization and the nonrelativistic Oppenheimer-Brinkman-Kramers calculations of Nikolaev (OBKN) [10] for electron capture. The ECPSSR cross sections were evaluated as described in [11] for direct ionization and in [12] for electron capture.

These theories were developed for fully-stripped projectiles; they are applied here with one modification in that the number of available states on the projectile is diminished due to the presence of the electrons on it. This narrows the electron-capture channel so that, even at the relatively large Z_1/Z_2 ratios, the direct ionization may still overshadow the electron capture contribution. No attempt is made to account for the screening of the projectile by its own electrons. Such screening plays a significant role [13] when $v_1 > v_{2S}$, but it is expected to be of a little consequence in the $v_1 < v_{2S}$ regime of interest for our experiments. Here, v_{2S} stands for the orbital velocity in the S = K or L shell.

The number of bound states on the projectile into which the electron can be captured has to be known to calculate the electron capture cross section for such a projectile. We estimate it in two ways: from the incident charge states of argon and from the effective charge that this projectile has in the target as given by eq. (B3) of Appendix B. For 36, 56.4, 76.6, and 103 MeV, the argon ions have the incident charge of 4, 5, 6, and 7, respectively; correspondingly, the effective charges were 12.6, 14.1, 15.0, and 15.8. Thus, if the incident charges were taken, then capture to only a fraction of the M-shell states on the projectile would be possible. Once the effective charge is assumed as the charge state of the projectile during the X-ray production, all M-shell states and as much as ~ 70% of the L-shell become available for electron capture. In the thick targets of our experiments, the dominant contribution to the observed X-rays occurs while the projectile is in the charge-state equilibrium. To the extent that the effective charge equals the charge state at equilibrium, we tend to favor it over the incident charge as a more realistic representation of our experimental conditions.

In figs. 4-9, the X-ray production cross sections σ_X (closed circles) extracted from the experimental σ_X^{obs} values (open circles) are compared with the predictions of the first Born approximation (dashed curves) and with the predictions of the ECPSSR theory (solid curves). The lower curves of each set correspond to the assumption that the incident charge is the charge of the projectile, while the upper curves represent the cases for which the charge of the projectile is taken to be its effective charge.

Agreement between the theoretical predictions and the solid data points is generally poor. This is to be expected, however, since both theories are inherently perturbative approaches in the ratio Z_1/Z_2, which is not small for the collision systems investigated in this work. The agreement improves as one goes from $Z_1/Z_2 = 0.78$ for $_{23}V$ (fig. 4) to $Z_1/Z_2 = 0.44$ for $_{41}Nb$ (fig. 6).

Although values of Z_1/Z_2 for the L-shell measurements are even smaller, the disagreement persists. To a great extent such a disagreement reflects the improper choice of the values for X-ray emission probabilities that are correct only for atoms in their ground states except for a single hole. When the fluorescence yields are as small as 0.2 -- as they are for the L-shells of $_{41}Nb$, $_{73}Ta$, $_{78}Pt$ and the K-shell of $_{23}V$ -- the multiple ionization of an atom may lead to drastic changes. By contrast, the K-shell fluorescence yields of $_{29}Cu$ (0.440) and $_{41}Nb$ (0.747) are not expected to change significantly.

The peaks in cross sections for ionization of L- and M-shells of the considered targets appear in the low-energy range of our data for K- and L-shells, respectively. It is there that the multiple ionization is most probable. Since the multiple ionizations always yield larger values for the X-ray emission probabilities than the single-hole values assumed in our conversion of ionization to X-ray production cross sections, the solid curves of ECPSSR theory should converge toward the solid data points (except for the Nb L X-rays which were subject to greater experimental difficulties) if the multiple-hole values were to be used instead. A calculation of the X-ray emission probabilities corrected for multiple ionization is needed to quantify this statement.

5. Summary and conclusions

We have measured K and L X-ray production cross sections in $_{23}V$, $_{29}Cu$, $_{41}Nb$, $_{73}Ta$, and $_{78}Pt$ by 36-103 MeV $^{40}_{18}Ar$ ions. The observed data are corrected for finite target thickness and, as such, compared with the predictions of available theories. The extracted data tend to agree with the ECPSSR theory as long as the major discrepancies are to be attributed to the multiple ionizations which can profoundly change the X-ray emission probabilities.

It appears that more X-ray production cross sections with sufficiently heavy and energetic ions are needed for a systematic analysis. We observe that such data should always be corrected for energy loss of the projectile and X-ray attenuation in the target. Comparison with theories of ionization hinges on detailed knowledge of the multiple ionization process. Comprehensive calculations of ionization cross sections in non-perturbative theories for the $Z_1/Z_2 > 0.5$ systems would also be of great interest.

It has been shown recently [19] that for some applications (for example, the analysis of Cl and S in polluted atmospheres), argon ions of 2-6 MeV incident energies are no better than the conventional 2 MeV protons in achieving certain levels of sensitivity. This is simply because the target K ionization cross sections are larger with protons than with the relatively slow argon ions. For targets in the mid-range of the periodic table, the inner shell vacancy production tends to peak when the projectile energy is a few MeV/u. When argon ions reach energies of the order of 100 MeV, the resulting X-ray output is much larger than the case with protons or

other light ions at any energy. On the basis of the present cross sections, we designed a successful experiment to study the influence of the chemical environment as manifested through intensity variations amongst the various satellite lines. These results are reported in Paper III. We have also initiated a broad program for measuring X-ray production cross sections for a number of target-projectile combinations taking advantage of the new Holifield Heavy Ion Research Facility at Oak Ridge.

We are indebted to C. B. Fulmer for carrying out the optical model calculations and to T. M. Rosseel for investigating the uniformity of the targets. This research was sponsored by the Division of Basic Energy Sciences, U.S. Department of Energy, under Contract No. W-7405-eng-26 with the Union Carbide Corporation.

Appendix A. Extraction of X-ray production cross sections

When $\overline{\Delta E}/E_1 << 1$, eq. (2) leads to [4]

$$\sigma_X^{obs}(E_1) = \frac{1-e^{-\mu' t'}}{\mu' t'} \sigma_X(E_1 - \overline{\Delta E}) \tag{A1}$$

where

$$\overline{\Delta E} = f(\mu' t') \cdot \overline{\Delta E_R} \tag{A2}$$

with $f(y) \equiv 2[1-(1+y)e^{-y}]/y(1-e^{-y}) < 1$, and $\overline{\Delta E_R} \equiv \frac{1}{2} S(E_1)\, t'$ is the stopping power S times the arithmetic average of the effective thicknesses at the entrance to and exit from the target. An analytical formula for S is given in Appendix B, eqs. (B1-B3).

Basbas et al. [4] proceed to extract σ_X by postulating the dependence $\sigma_X = cE^{\ell}$ on the projectile energy with suitable constants c and ℓ. The σ_X is derived in this method after division, among other factors, by $(1-\overline{\Delta E}/E_1)^{\ell}$. We find this procedure to be inadequate in our analysis because when $\overline{\Delta E}/E_1$ becomes as large as 0.2, the accurate knowledge of ℓ is of crucial importance. One notes that both c and ℓ are energy dependent if more than one experimental energy is considered and, therefore, the ℓ cannot be uniquely defined.

To circumvent this ambiguity, we - rather than relating $\sigma_X^{obs}(E_1)$ to $\sigma_X(E_1)$ - deduce directly from eq. (A1) that

$$\sigma_X(E_1 - \overline{\Delta E}) = C_X\, C_R\, \sigma_X^{obs}(E_1), \tag{A3}$$

where

$$C_X \equiv \mu' t' / (1 - e^{-\mu' t'}) \tag{A4}$$

and

$$C_R \equiv 1 / (1 - \overline{\Delta E}_R / E_1)^2 \tag{A5}$$

correct the observed X-ray production cross section, respectively, for the x-ray self-attenuation and for the Rutherford scattering so that $(d\sigma/d\Omega)_p$ is in fact evaluated at $E_1 - \overline{\Delta E_R}$ instead of E_1 as in eq. (1). The cross sections calculated from eq. (A3) are the cross sections to be compared with theoretical predictions at an incident energy $E_1 - \overline{\Delta E}$.

Appendix B. An analytical forumla for stopping power

The average energy lost by the projectile, $\overline{\Delta E}$[MeV] of eq. (A2), in the target of thickness t[mg/cm^2] is proportional to the electronic stopping power S[MeV·cm^2/mg]. In the target whose element is characterized by the atomic number Z_2 and atomic mass A_2, the stopping power for the projectile of velocity $v_1 = 6.35\ (E_1/A_1)^{1/2}$, with E_1/A_1 in MeV/u, and effective charge Z_1^* can be written as

$$S = \frac{5.77}{A_2}\left(\frac{Z_1^*}{x}\right)^2 L(x), \qquad (B1)$$

where $x \equiv v_1/(Z_2)^{1/2}$.

Lindhard and Scharff [14] derived the dimensionless reduced stopping power function L(x) as (see eq. (11) of [14])

$$L(x) = 1.36x^{1/2} - 0.016x^{3/2} \qquad (B2)$$

and showed it to be in good agreement with the stopping power data for protons, $Z_1^* = 1$, of sufficiently small velocities, i.e., when $x < 10$. The maximum value of x in our experiments is 4.5 in stopping a 103-MeV ^{40}Ar beam in a $_{23}$V target. The main problem of applying Eq. (B1) to our collision systems lies in the choice of the effective charge for argon ions. There is no <u>ab initio</u> theory for the effective charge to be used in eq. (B1).

We choose to follow the prescription of Brandt [15] who calculated Z_1^*, on the basis of the Bohr stripping criterion, for a Thomas-Fermi atom. In this model Z_1^*/Z_1 is a universal function of $y \equiv (v_1/Z_1^{2/3})/b$, where b is

an adjustable parameter. We approximate the tabular values of [15] to within 2% as

$$\frac{Z_1^*}{Z_1} = \frac{y^{3/2}}{(0.026 + 0.75y + 0.17y^2 + y^3)^{1/2}} \qquad \text{(B3)}$$

and fix b = 1.26 as recommended [15,16] for relatively light projectiles such as argon.

Equation (B3) yields the values that are comparable with the results of the empirical formula of Ziegler [17]. For the projectile-target systems in our range of energies, the stopping power evaluated by eqs. (B1-B3) falls somewhat below Ziegler's empirical curves [18]. This discrepancy, however, rarely exceeds 10% and often is within the 5% margin of accuracy assigned by Ziegler to his own compilation. For the purposes of this work an analytical formula is more expedient than a semiempirical approach. Five percent uncertainties in stopping powers so calculated are acceptable since the variations in the target thickness exceed 5%.

[1] C.H. Rutledge and R.L. Watson, At. Data Nucl. Data Tables 12 (1973) 195; R.K. Gardner and T.J. Gray, At. Data Nucl. Data Tables 21 (1978) 515 and 24 (1979) 281; H. Paul, At. Data Nucl. Data Tables 24 (1979) 243 and Nucl. Instrum. Methods 192 (1982) 11.

[2] X-ray mass attenuation coefficients were compiled independently by W.H. McMaster, N. Kerr Del Grande, J.H. Mallett, and J.H. Hubbell, Compilation of X-ray cross sections, Lawrence Radiation Laboratory (Livermore) Report UCRL-50174 Sec. II, Rev. 1 (1969); and E. Storm and H.I. Israel, Nucl. Data Tables A7 (1970) 565. See also J.H. Hubbell et al., in International Tables for X-ray Crystallography (Kynoch Press, Birmingham, 1974) Vol. 4, p. 47; and E.C. Montenegro, G.B. Baptista, and P.W.E.P. Duarte, At. Data Nucl. Data Tables 22 (1978) 131. The self-attenuation coefficients are subject to greatest uncertainties because the X-rays originate at or near X-ray absorption edges; a 15% uncertainty could be assigned to these coefficients. Their numerical values, therefore, are quoted with only two significant figures as obtained by private communication from John H. Hubbell of the National Bureau of Standards. These relatively large uncertainties result in at most 1% errors in the evaluation of C_x (see Appendix A, eq. A3).

[3] C.B. Fulmer, Oak Ridge National Laboratory, private communication.

[4] G. Basbas, W. Brandt, and R. Laubert, Phys. Rev. A 17 (1978) 1655.

[5] J.A. Tanis, W.W. Jacobs, and S.M. Shafroth, Phys. Rev. A 22 (1980) 483.

[6] T.M. Rosseel, Oak Ridge National Laboratory, private communication.

[7] M.O. Krause, J. Phys. Chem. Ref. Data 8 (1979) 307.

[8] J.H. Scofield, Phys. Rev. A 10 (1974) 1507 and in Atomic Inner Shell Processes edited by B. Crasemann (Academic Press, New York, 1975), Vol. I, p. 265.

[9] G.S. Khandelwal, B. -H. Choi, and E. Merzbacher, At. Data 1 (1969) 103 the L-shell tables were superseded by B. -H. Choi, E. Merzbacher, and G.S. Khandelwal, ibid. 5 (1973) 291; the K-shell tables were extended by R. Rice, G. Basbas, and F.D. McDaniel, At. Data Nucl. Data Tables 20 (1977) 503.

[10] V.S. Nikolaev, Zh. Eksp. Teor. Fiz. 51 (1966) 1263 [Sov. Phys. JETP 24 (1967) 847.

[11] W. Brandt and G. Lapicki, Phys. Rev. A 23 (1981) 1717.

[12] G. Lapicki and F.D. McDaniel, Phys. Rev. A 22 (1980) 1896; (E) Phys. Rev. A 23 (1981) 975. To account for the energy-loss effect, as in direct ionization calculations of [11], exact minimum momenta transfer, instead of eq. 3 of [12] is used in our present calculations for electron capture.

[13] F.K. Chen, G. Lapicki, R. Laubert, S.B. Elston, R.S. Peterson, and I.A. Sellin, Phys. Lett. 60A (1977) 292; L.H. Toburen, P. Ziem, N. Stolterfoht, D. Schneider, and M. Prost, IEEE Trans. Nucl. Sci. 28 1981) 1131.

[14] J. Lindhard and M. Scharff, K. Dan. Vidensk. Selsk, Mat. -Fys. Medd. 27 (1953) No. 15.

[15] W. Brandt in Atomic Collisions in Solids (Plenum, New York, 1975), Vol. I, p. 261.

[16] B.S. Yarlagadda, J.E. Robinson, and W. Brandt, Phys. Rev. B 17 (1978) 3473.

[17] J. Ziegler, Appl. Phys. Lett. 31 (1977) 544.

[18] J.F. Ziegler, Stopping Cross-sections for Energetic Ions in all Elements, Vol. 5 of The Stopping and Ranges of Ions in Matter edited by J. F. Ziegler (Pergamon, New York, 1979).

[19] Ch. Heitz, J. Cailleret, J. Iturbe, G. Lagarde, and P. Siffert, Nucl. Instrum. Methods 191 (1981) 558.

Table 1. For the various targets (thickness, t, in mg/cm^2 listed just below each element; $t'=\sqrt{2}t$), the average energy loss ($\overline{\Delta E_R}$) experienced by the $^{40}_{18}Ar$ projectile relative to its incident energy (36.0, 56.4, 76.6, and 103 MeV), and the self-attenuation mass coefficient ($\mu=\mu'$) in cm^2/mg derived from [2] are listed for insertion into eq. (2).

	^{23}V (0.830)	^{29}Cu (0.887)	^{41}Nb (0.744)	^{73}Ta (0.957	^{78}Pt (0.927)
$\overline{\Delta E_R}/36.0$	0.221	0.214	0.146	0.130	0.121
$\overline{\Delta E_R}/56.4$	0.144	0.140	0.096	0.085	0.079
$\overline{\Delta E_R}/76.6$	0.104	0.101	0.070	0.062	0.058
$\overline{\Delta E_R}/103$	0.074	0.073	0.050	0.045	0.042
$\mu(K_\alpha)$	0.096	0.052	0.020		
$\mu(K_\beta)$	0.074	0.039	0.014		
$\mu(L_\ell)$				0.220	0.180
$\mu(K_{\alpha 1})$				0.160	0.130
$\mu(L_{\beta 1})$				0.110	0.085
$\mu(L_{\alpha 1}+L_{\beta 1})$			0.700		

Table 2. Observed K X-ray production cross sections, σ_X^{obs}, measured at E_1, and corrected cross sections, σ_X at $E_1-\overline{\Delta E}$, for targets of V, Cu, and Nb bombarded with 36-103 ^{40}Ar ions.

Target	E_1 (MeV)	σ_X^{obs} (barns)		$E_1-\overline{\Delta E}$ (MeV)	σ_X (barns)	
		K_α	K_β		K_α	K_β
$_{23}V$	36.0	1.00×10^3	8.40×10^1	28.2	1.75×10^3	1.44×10^2
	56.4	8.19×10^3	7.73×10^2	48.4	1.18×10^4	1.10×10^3
	76.6	1.70×10^4	1.86×10^3	68.8	2.25×10^4	2.42×10^3
	103	2.32×10^4	2.80×10^3	95.5	2.86×10^4	3.41×10^3
$_{29}Cu$	36.0	2.36×10^1	1.83×10^0	28.4	3.94×10^1	3.03×10^0
	56.4	4.45×10^2	4.80×10^1	48.6	6.23×10^2	6.66×10^1
	76.6	1.44×10^3	1.75×10^2	68.9	1.84×10^3	2.22×10^2
	103	3.65×10^3	4.85×10^2	95.6	4.38×10^3	5.78×10^2
$_{41}Nb$	36.0	3.24×10^{-1}	9.21×10^{-3}	30.7	4.49×10^{-1}	1.27×10^{-2}
	56.4	4.49×10^0	6.41×10^{-1}	51.0	5.55×10^0	7.88×10^{-1}
	76.6	1.51×10^1	2.30×10^0	71.3	1.77×10^1	2.68×10^0
	103	5.77×10^1	1.15×10^1	97.9	6.46×10^1	1.29×10^1

Table 3. Observed L X-ray production cross sections, σ_X^{obs}, measured at E_1, and corrected cross sections, σ_X at $E_1-\overline{\Delta E}$, for targets of Nb, Ta, and Pt with 36-103 MeV $^{40}_{18}Ar$ ions.

Target	E_1 (MeV)	σ_X^{obs} (barns) L_α	L_β	L_ℓ	$E_1-\overline{\Delta E}$ (MeV)	σ_X (barns) L_α	L_β	L_ℓ
		$L_{\alpha+\beta}$				$L_{\alpha+\beta}$		
$_{41}Nb$	36.0	1.42×10^4			31.4	2.74×10^4		
	56.4	4.26×10^4			51.7	7.37×10^4		
	76.6	4.50×10^4			71.9	7.36×10^4		
	103	7.51×10^4			98.5	1.18×10^5		
$_{73}Ta$	36.0	2.55×10^2	5.73×10^1	1.16×10^1	31.5	3.75×10^2	8.15×10^1	1.77×10^1
	56.4	1.74×10^3	5.18×10^2	5.95×10^1	51.8	2.31×10^3	6.66×10^2	8.21×10^1
	76.6	2.96×10^3	8.81×10^2	1.45×10^2	72.0	3.73×10^3	1.08×10^3	1.90×10^2
	103	7.00×10^3	2.30×10^3	3.61×10^2	98.6	8.54×10^3	2.72×10^3	4.58×10^2
$_{78}Pt$	36.0	1.14×10^2	2.27×10^1	5.26×10^0	31.8	1.61×10^2	3.11×10^1	7.64×10^0
	56.4	7.80×10^2	2.23×10^2	3.91×10^1	52.1	1.00×10^3	2.76×10^2	5.18×10^1
	76.6	1.84×10^3	4.44×10^2	9.78×10^1	72.3	2.26×10^3	5.30×10^2	1.23×10^2
	103	4.07×10^3	1.15×10^3	2.15×10^2	98.8	4.83×10^3	1.33×10^3	2.63×10^2

Table 4. Experimental uncertainties for a typical data point. Numerical values used in obtaining the observed K_α X-ray cross section, σ_X^{obs}, and the corrected cross section, σ_X, for a ^{41}Nb target irradiated with ^{40}Ar at 76.6 MeV. Uncertainties are listed in percent of the measured or deduced quantity.

Quantity	Value	% Error
Number of X-ray counts, N_X	3.10×10^3	1.8
Number of particle counts, N_P	1.09×10^5	0.3
Livetime of X-ray detector, τ_X	8.30×10^2 s	2.0
Livetime of particle detector, τ_P	1.12×10^3 s	0.5
Efficiency of X-ray detector, ε_X	8.87×10^{-5}	7.0
Rutherford cross section, $(d\sigma/d\Omega)_{P(LAB)}$	14.67 b/sr	
Solid angle of particle detector, $\Delta\Omega$	2.38×10^{-3} sr	2.0
Target thickness, t	0.744 mg/cm^2	7.0
X-ray self-attenuation mass coefficient, μ	0.020 cm^2/mg	15.0
Correction for self attenuation, C_X, eq. (A4)	1.011	0.2
Stopping power, S, eqs. (B1-3)	10.2 MeV cm^2/mg	5.0
Correction for Rutherford scattering, C_R, eq. (A5)	1.156	18.5
Observed X-ray cross section, σ_X^{obs}, eq. (1)	15.1 b	7.8
X-ray production cross section σ_X, eq. (A3), corrected for finite target thickness	17.7 b	20.1

TABLE V. X-ray emission probabilities for the L shell used in eq. (3).

Element	L	ν_L^{L1}	ν_L^{L2}	ν_L^{L3}
Nb	$\alpha_1 + \beta_1$	~ 0.0325	~ 0.0325	~ 0.0325
Ta	$\alpha_1 + \beta_1 + \ell$	0.118	0.233	0.183
Pt	$\alpha_1 + \beta_1 + \ell$	0.153	0,283	0.227

Fig. 1. Schematic (not to scale) diagram of the experimental arrangement.

Fig. 2. Typical spectra of X-rays from the $^{40}_{18}Ar$ projectiles and from metal targets of vanadium, copper, niobium, tantalum, and platinum at an $^{40}_{18}Ar$ energy of 36.0 MeV.

Fig. 3. Typical spectra of X-rays from the $^{40}_{18}Ar$ projectiles and from metal targets of vanadium, copper, niobium, tantalum, and platinum at an $^{40}_{18}Ar$ energy of 103 MeV.

Fig. 4. $K \equiv K_\alpha + K_\beta$ X-ray production in vanadium by argon ions. The open circles show the observed X-ray production cross sections, Eq. (1). The closed circles represent X-ray production cross sections after corrections for finite target thickness, Eq. (A3). The curves are from the predictions of ionization (direct ionization + electron capture) theories multiplied by single-hole, X-ray emission probabilities. The dashed curves represent the first Born approximation of [9] and [10], and the solid curves are the predictions of the ECPSSR theory of [11] and [12]; the upper curves in each set are based on the effective charge for the projectile of eq. (B3); the lower curves in each set are calculated for the case when the projectile is assumed to remain in its incident charge.

Fig. 5. $K \equiv K_\alpha + K_\beta$ X-ray production in copper by argon ions. The meaning of the symbols and curves is the same as in fig. 4. Closed triangles depict values of cross sections corrected to vanishing target thickness for production of K X-rays by chlorine-ion bombardment of copper

(from [5]), as a function of the chlorine projectile energy expressed as MeV/u for comparison with the data from this work. The dash-dot curve is to guide the eye. To make an absolute comparison, the chlorine data should be shifted upwards by ~ 12% since the cross sections, to first order, should scale as Z_1^2.

Fig. 6. $K \equiv K_\alpha + K_\beta$ X-ray production in niobium by argon ions. The meaning of the symbols and curves is the same as in fig. 4. Good agreement between the solid points and curves is obtained because $Z_1/Z_2 = 0.44$ and the single-hole fluorescence yield 0.747 of [7] is insignificantly influenced by multiple ionizations.

Fig. 7. $L_{\alpha_1} + L_{\beta_1}$ X-ray production in niobium by argon ions. The meaning of the symbols and curves is the same as in fig. 4. Additional difficulties arose in the analysis of the data because of the proximity of the Ar K X-rays (see figs. 2 and 3).

Fig. 8. $L_{\alpha_1} + L_{\beta_1} + L_\ell$ X-ray production in tantalum by argon ions. The meaning of the symbols and curves is the same as in fig. 4.

Fig. 9. $L_{\alpha_1} + L_{\beta_1} + L_\ell$ X-ray production in platinum by argon ions. The meaning of the symbols and curves is the same as in fig. 4.

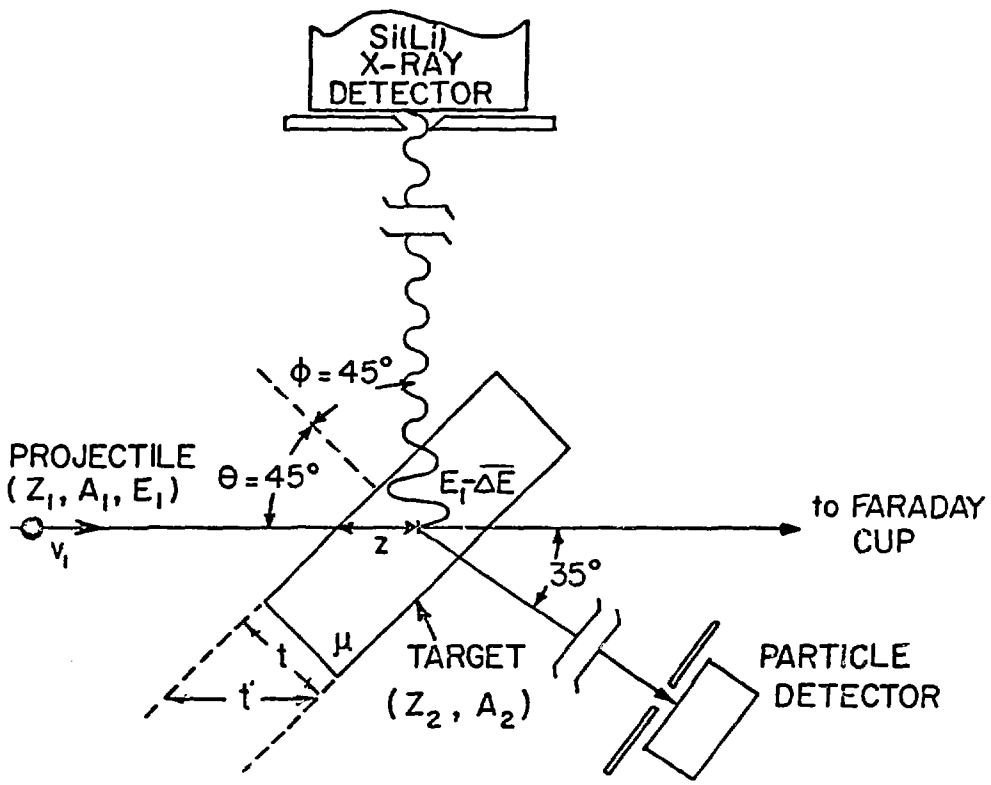
Si(Li)
X-RAY
DETECTOR
$\phi = 45°$
PROJECTILE
(Z_1, A_1, E_1)
$\theta = 45°$
$E_1 - \overline{\Delta E}$
to FARADAY
CUP
v_1
z
35°
t
μ
t'
TARGET
(Z_2, A_2)
PARTICLE
DETECTOR

Figure 1

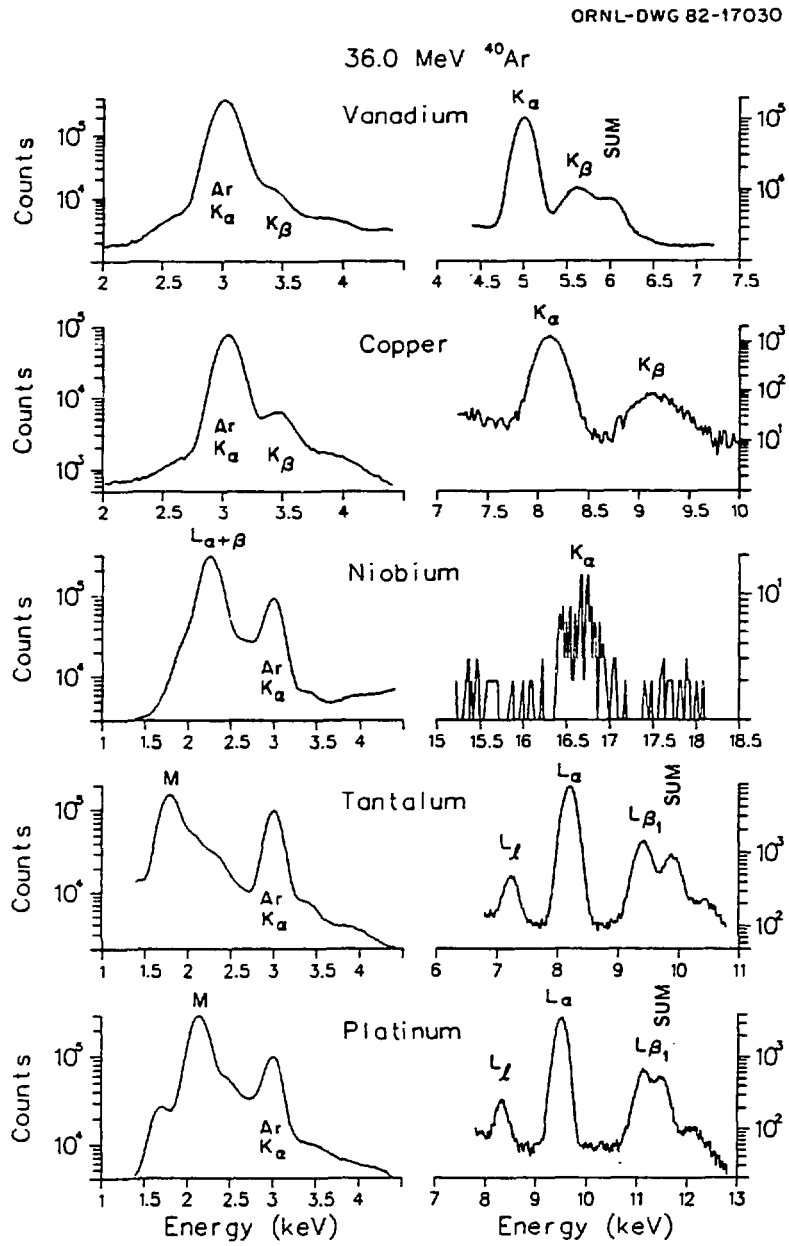
ORNL-DWG 82-17030
36.0 MeV ^{40}Ar
Vanadium
Copper
Niobium
Tantalum
Platinum
Counts
Ar Kα
Kβ
Kα
SUM
Lα+β
M
Lα
Lβ1
Lℓ
Energy (keV)

Figure 2

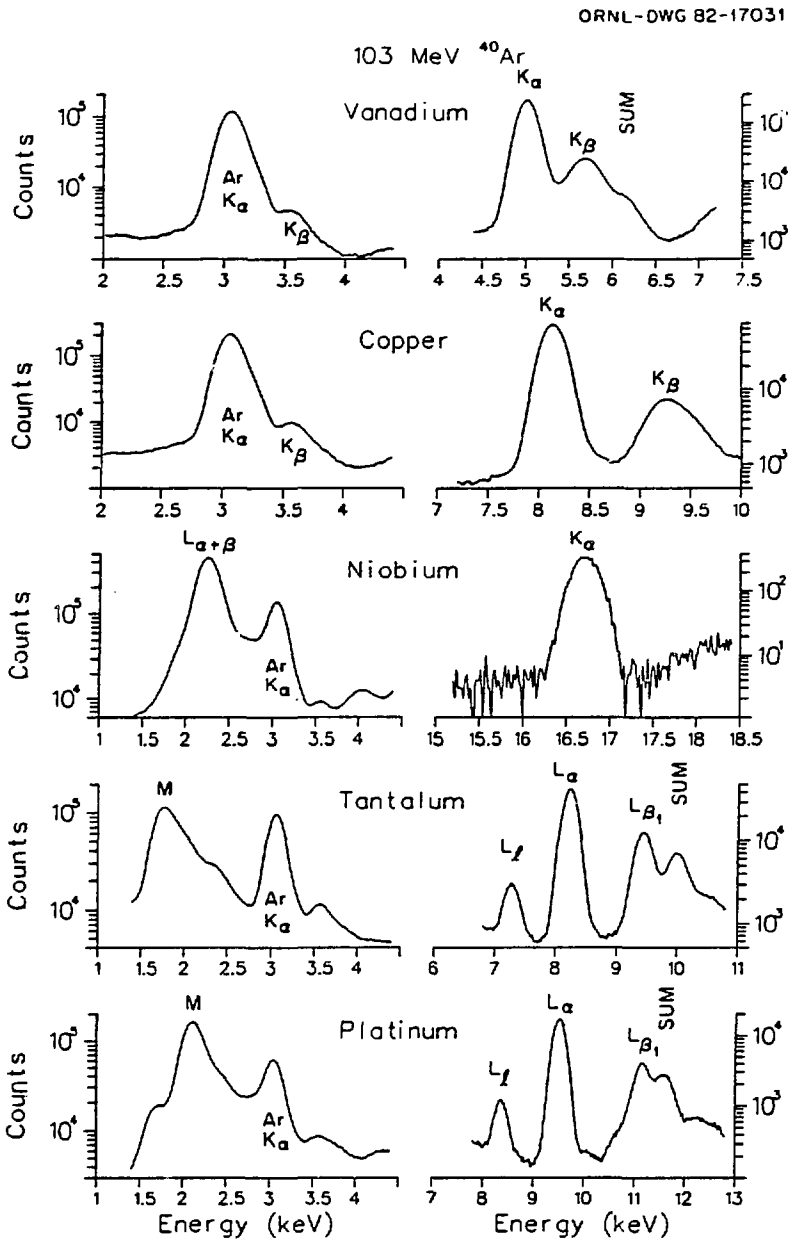
ORNL-DWG 82-17031
103 MeV ^{40}Ar
Vanadium
Copper
Niobium
Tantalum
Platinum
Counts
Ar Kα
Kβ
Kα
SUM
Lα+β
Lα
Lβ1
Ll
M
Energy (keV)

Figure 3

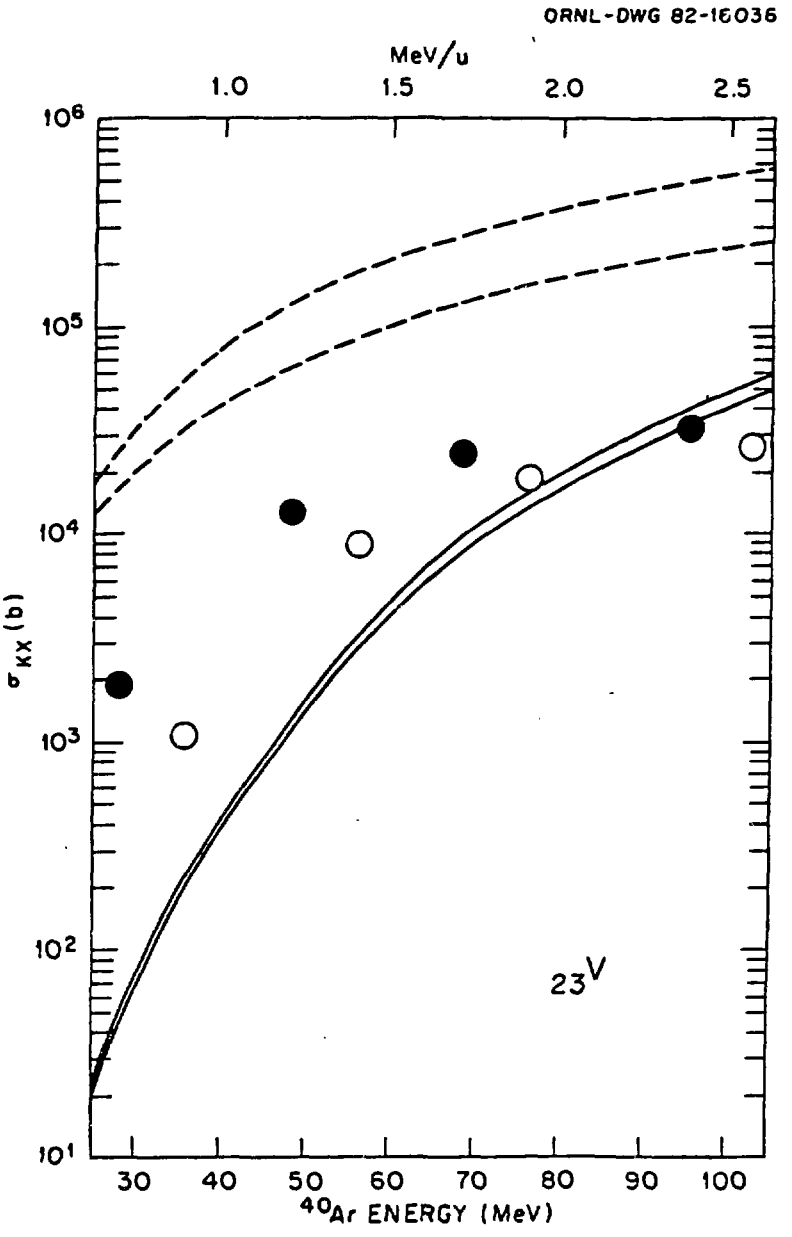
ORNL-DWG 82-16036
MeV/u
1.0
1.5
2.0
2.5
10^6
10^5
10^4
10^3
10^2
10^1
σ_{KX} (b)
^{23}V
30
40
50
60
70
80
90
100
^{40}Ar ENERGY (MeV)

Figure 4

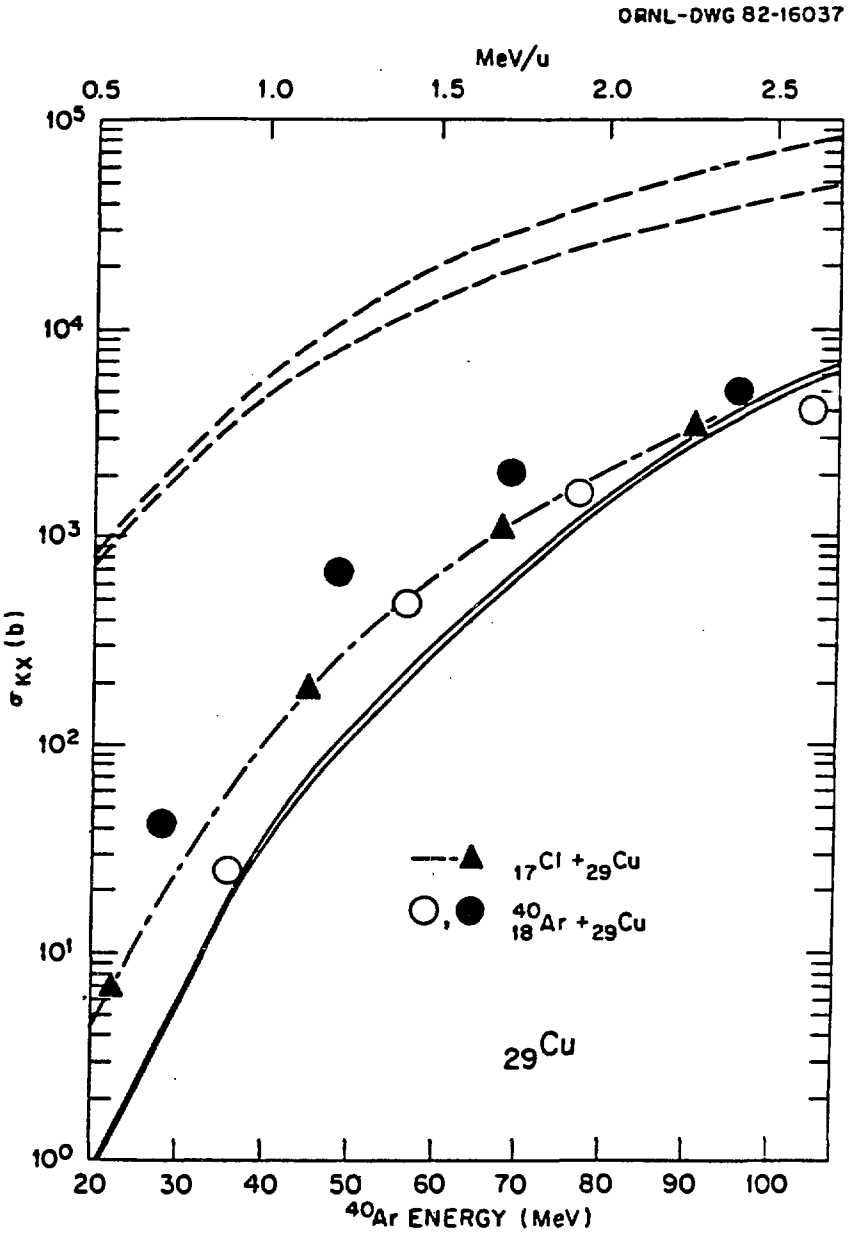
ORNL-DWG 82-16037
MeV/u
0.5
1.0
1.5
2.0
2.5
10^5
10^4
10^3
10^2
10^1
10^0
σ_{KX} (b)
$_{17}Cl + _{29}Cu$
$^{40}_{18}Ar + _{29}Cu$
$_{29}Cu$
20
30
40
50
60
70
80
90
100
^{40}Ar ENERGY (MeV)

Figure 5

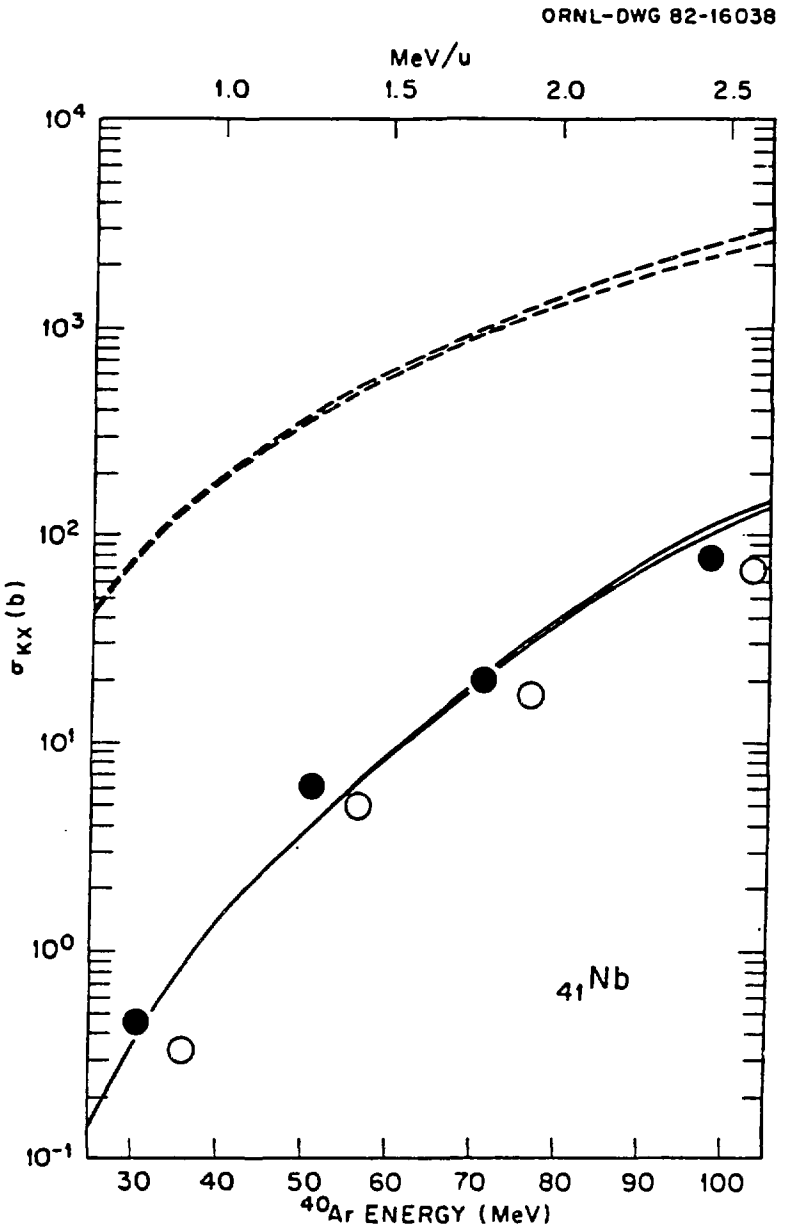
ORNL-DWG 82-16038
MeV/u
1.0
1.5
2.0
2.5
10^4
10^3
10^2
10^1
10^0
10^{-1}
σ_{KX} (b)
$_{41}$Nb
30
40
50
60
70
80
90
100
^{40}Ar ENERGY (MeV)

Figure 6

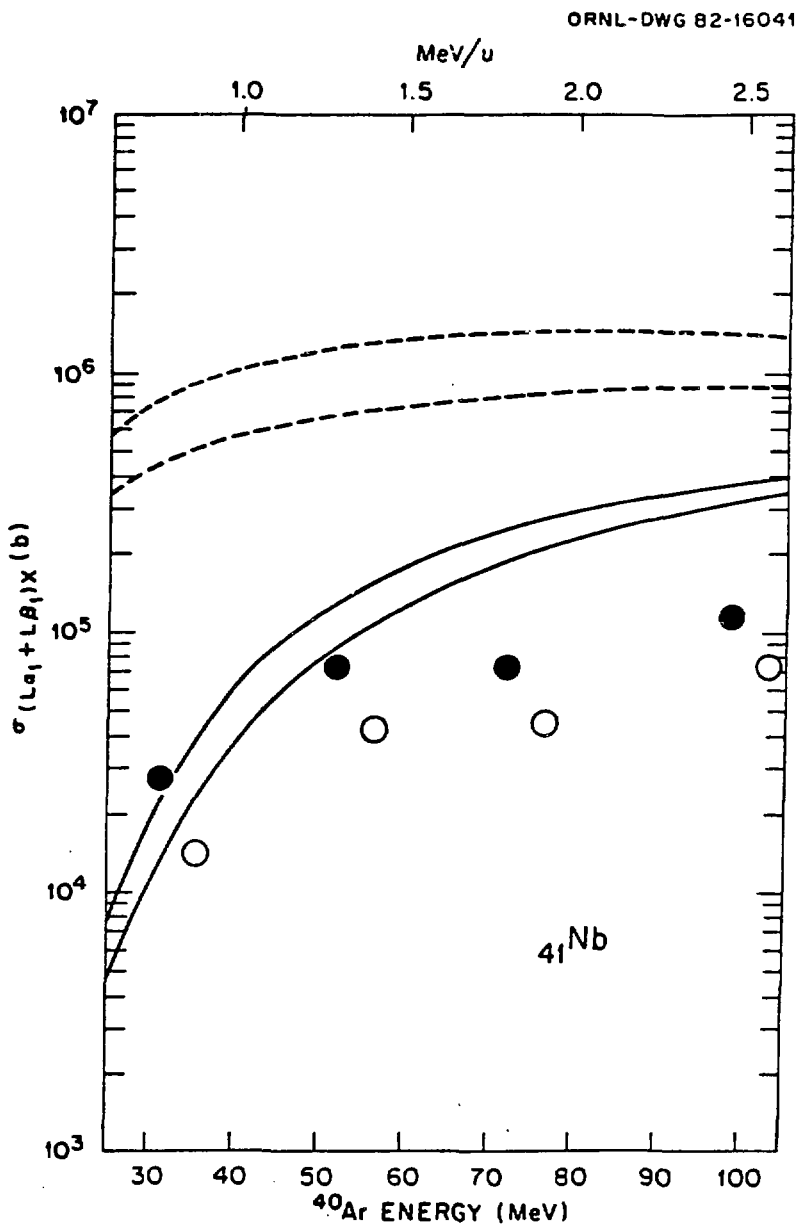
ORNL-DWG 82-16041
MeV/u
1.0
1.5
2.0
2.5
10^7
10^6
10^5
10^4
10^3
$\sigma_{(La_1+L\beta_1)X}$ (b)
$_{41}Nb$
30
40
50
60
70
80
90
100
^{40}Ar ENERGY (MeV)

Figure 7

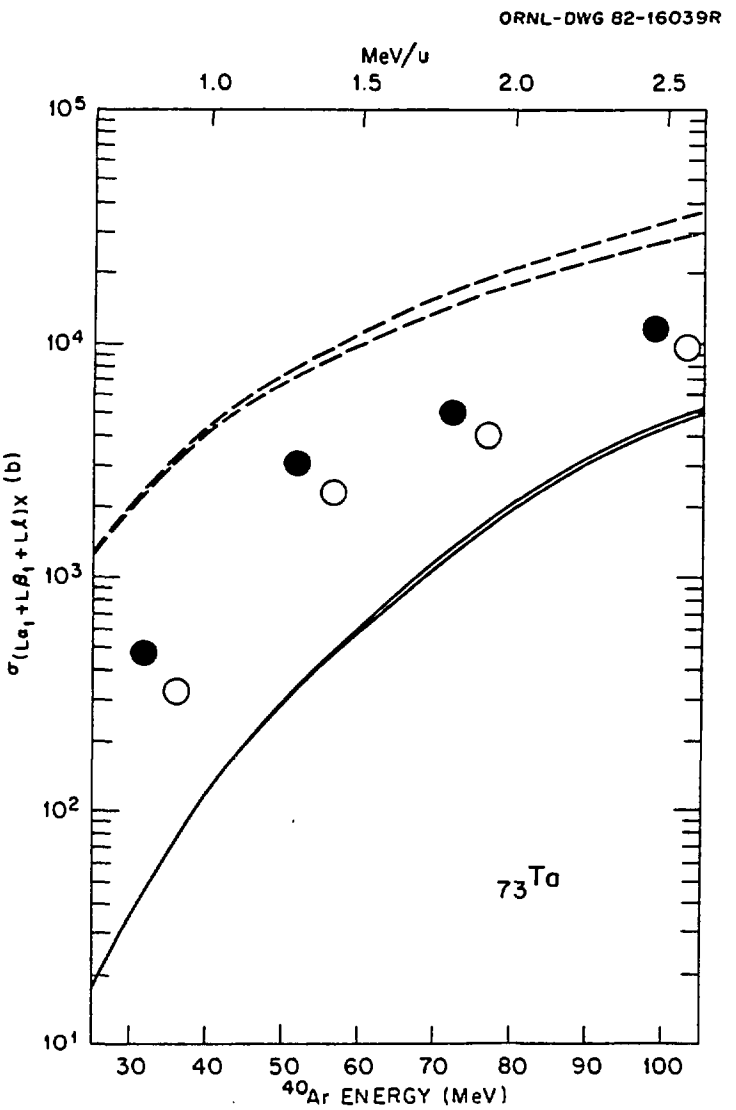
ORNL-DWG 82-16039R
MeV/u
1.0
1.5
2.0
2.5
10^5
10^4
10^3
10^2
10^1
$\sigma_{(L\alpha_1+L\beta_1+L\ell)X}$ (b)
$_{73}$Ta
30
40
50
60
70
80
90
100
^{40}Ar ENERGY (MeV)

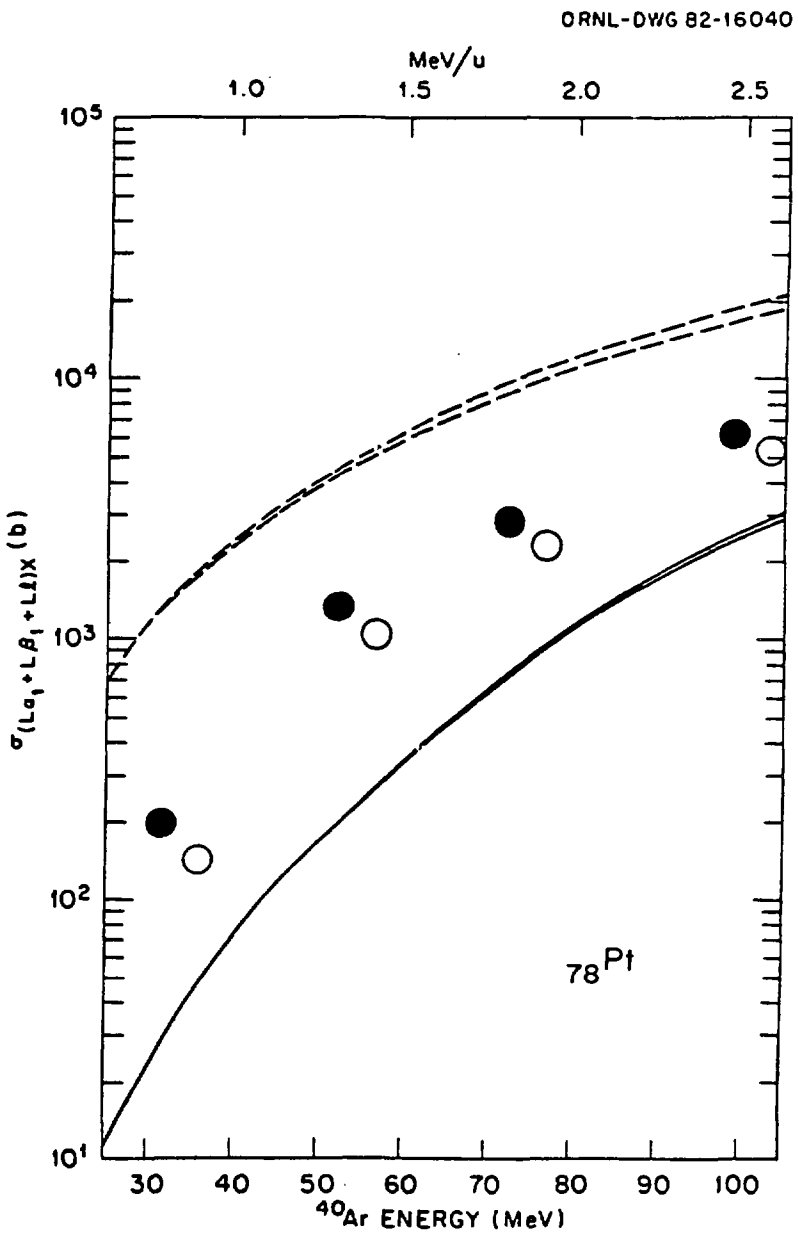
ORNL-DWG 82-16040
MeV/u
1.0
1.5
2.0
2.5
10^5
10^4
10^3
10^2
10^1
$\sigma_{(L\alpha_1+L\beta_1+L\ell)X}$ (b)
$_{78}$Pt
30
40
50
60
70
80
90
100
^{40}Ar ENERGY (MeV)

Figure 9

DISCLAIMER